

# Fast quantum transfer mediated by topological domain walls

Juan Zurita

*Instituto de Ciencia de Materiales de Madrid (CSIC), Cantoblanco, E-28049 Madrid, Spain and  
Departamento de Física de Materiales, Universidad Complutense de Madrid, E-28040 Madrid, Spain\**

Charles E. Creffield

*Departamento de Física de Materiales, Universidad Complutense de Madrid, E-28040 Madrid, Spain\**

Gloria Platero

*Instituto de Ciencia de Materiales de Madrid (CSIC), Cantoblanco, E-28049 Madrid, Spain*

Transfer protocols in 1D topological models are usually implemented between the left and right end modes of the system, and their speed often exponentially reduces with transfer distance. In this work, we propose a way to harness the localization properties of a multidomain Creutz ladder, a flat-band topological model with two protected states per domain wall, to choose the two modes along the ladder which will be swapped using a transfer protocol. Only protected states are involved in the transfer, and so it is robust against symmetry-preserving disorder. Remarkably, one protected state per domain wall is left undisturbed, even if it is located between the two swapped states. An effective 1D chain of protected states is then established, where any pair of them can be swapped without affecting the others, providing a versatile and resilient platform for quantum information purposes. Additionally, we propose transfer protocols in multidomain Creutz ladders and SSH chains which exponentially speed up the process with respect to their single-domain counterparts, thus reducing the accumulation of errors and drastically increasing their performance, even in the presence of symmetry-breaking disorder.

## I. INTRODUCTION

We are currently experiencing the NISQ era of quantum computing [1], where noisy, intermediate-scale quantum processors start to show the first signs of quantum advantage. The path ahead towards large error-correcting codes and, eventually, fault-tolerant quantum computation will most likely require a wide array of tools and techniques to fight decoherence. One of these techniques can be the use of symmetry-protected states in topological insulators, which are specially robust against some types of noise, and are already available in the laboratory.

These topological boundary states naturally decouple from the bulk of the system, and thus form an invariant subspace of the Hamiltonian around zero energy, which has support on the boundaries of the material. This allows us to define quantum information protocols in 2D [2–5] and 1D [6–20] which transport a particle from one region of the boundary to another, with little to no loss to the bulk, even in noisy regimes. These *particle* transfer protocols can then be used in different ways to implement *state* transfer protocols –for example, using these particles (e.g. photons) as a communication line between distant qubits [7], or building a quantum computer with specific couplings so that its qubit states are equivalent to the empty ( $|0\rangle$ ) and filled ( $|1\rangle$ ) states of a topological Hamiltonian [10]– or other remote quantum operations [7, 11]. In this work we are mainly concerned with

the particle transfer states in the topological systems we study, leaving their specific applications in quantum information protocols for future works.

In particular, we investigate the possibilities of particle control provided by magnetic interference in the Creutz ladder (CL) [21], a quasi-1D topological insulator which was recently realized in three different cold atom systems [22–24], and can also be implemented with state-of-the-art technology in superconducting circuits [25, 26] (in which a CL plaquette has been implemented) and photonic lattices [27]. In a particular regime, an orthogonal basis of spatially compact energy eigenstates can be found, something associated with the complete flattening of both bands in momentum space. This phenomenon is called Aharonov-Bohm caging [28–31], and it is caused by the destructive interference of paths due to the magnetic Peierls phases. Flat band models are interesting playgrounds to study the effects of interactions and disorder [32–36], and, like topological models, also show interesting properties for quantum information purposes [37, 38]. In a Creutz ladder with multiple topological domains, where each domain wall can hold up to two protected states, it can allow us to decouple some of the boundary states of the system from all the others at will.

Remarkably, if this is done to a state in a two-state domain wall, its partner can be used to leapfrog over it, thus allowing the transfer of a particle through the wall while leaving the decoupled state undisturbed and protected inside it. Even though the CL topological phase diagram is well-known [39, 40], the properties of its possible domain walls have not been studied in the literature, to the best of our knowledge.

Additionally, we tackle a well-known issue in protocols

---

\* jzurita@ucm.es

that involve the hybridization of exponentially decaying end modes, which is the –also exponential– increase in the time of transfer as a function of system length. A solution for this problem can be found in multidomain models, in which the protected states in domain walls along the system can act as signal amplifiers, exponentially decreasing the transfer time between distant states even with the most simple control protocols. After studying the case of the Creutz ladder, we also include a version of these exponentially accelerated transfer protocols for the SSH chain, a 1D model which is much easier to implement experimentally, and where each domain wall can only hold one boundary state. Domain walls in the SSH chain and related models have been studied since its inception [13, 41–44], and other transfer protocols using them exist in the literature [43], but our proposal have not been yet explored, as far as we know.

In Section II, we present the multidomain Creutz ladder, study its protected states and describe the possible transfer protocols that can be implemented in it. Then, we explore the exponentially accelerated transfer protocols that can be obtained using domain walls as signal amplifiers, both in the CL (Section III) and in the SSH chain (Section IV), as well as their resistance against disorder.

## II. MULTIDOMAIN CREUTZ LADDER

### A. Topological phases in the Creutz ladder

We consider an imbalanced Creutz ladder Hamiltonian:

$$\begin{aligned} \mathcal{H} = & - \sum_{j=1}^{L-1} \sum_{\sigma=A,B} \left[ J \xi_{j,\sigma} c_{j+1,\sigma}^\dagger c_{j,\sigma} + J c_{j+1,\bar{\sigma}}^\dagger c_{j,\sigma} + h.c. \right] \\ & + \sum_{j=1}^L \sum_{\sigma=A,B} s_\sigma \epsilon_j c_{j,\sigma}^\dagger c_{j,\sigma} \end{aligned} \quad (1)$$

where  $j = 1, \dots, L$  labels the different rungs,  $\sigma = A, B$  designates the two legs, with  $\bar{A} = B$  and vice versa,  $\xi_{j,\sigma} = e^{i s_\sigma \phi_j / 2}$ , with  $s_\sigma = \delta_{\sigma,A} - \delta_{\sigma,B}$ ,  $\phi_j$  is the magnetic flux in the  $j$ -th plaquette,  $J$  is the horizontal and diagonal hopping amplitude and  $2\epsilon_j$  is the energy imbalance between the two legs in the  $j$ -th rung [see Fig. 1 (a)]. Operators  $c_{j,\sigma}^\dagger$  create a particle, which can be bosonic or fermionic, in site  $j, \sigma$ .

In a ladder with  $\epsilon_j = \epsilon$ ,  $\phi_j = \phi$  for all values of  $j$ , the topology of the system depends on  $\phi$  and  $\epsilon/J$ , as can be seen in Fig. 1 (b). The system has two distinct nontrivial phases when  $\epsilon < 2J$ , with winding numbers  $\nu = \pm 1$ , depending on the value of  $\phi$ , and a single trivial phase ( $\nu = 0$ ) when  $\epsilon > 2J$  [31, 39, 46]. When in a topological phase, topological zero modes appear in the ends of the ladder.

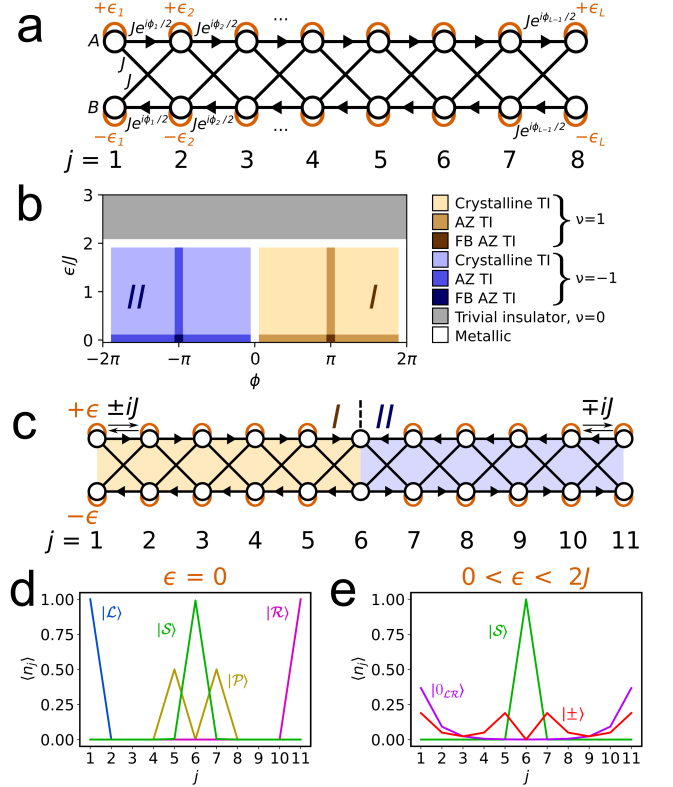


Figure 1. (a) Imbalanced Creutz ladder in the most general case. The energy imbalance parameters  $\epsilon_j$  and the magnetic Peierls phases  $\phi_j$  determine the topology, and can be used to define different domains. All hopping amplitudes have an additional minus sign. (b) Topological phase diagram of the imbalanced Creutz ladder. It is divided into two topological phases with winding numbers  $\nu = \pm 1$ , and a trivial phase with  $\nu = 0$ . The topology of the crystalline TI regions are not described by the standard Altland-Zirnbauer symmetry classes [45]. Those who can are marked with “AZ”. The flat-band points are labeled “FB”. (c) Two-domain Creutz ladder with no imbalance in its domain wall ( $\epsilon_6 = 0$ ), and with an energy imbalance parameter equal to  $\epsilon$  in all other rungs. This model has four topological states: the left and right end modes, and two states at the domain wall. (d) Spatial distribution of the AB-caged topological states in a two-domain Creutz ladder with  $\epsilon = 0$ : left, right and  $\mathcal{S}$ - and  $\mathcal{P}$ -type states. All of them are compact and pinned at zero energy. (e) Spatial distribution of the topological states in the system in (c), for  $\epsilon = J$ . A pair of antibonding and bonding states  $|\pm\rangle$  appear with small, opposite energies, while the other two states remain at zero energy.

Furthermore, the wall between domains that belong to different phases, with winding numbers  $\nu_1$  and  $\nu_2$ , will hold  $|\Delta\nu|$  zero modes, where  $\Delta\nu = \nu_2 - \nu_1$ . Due to the particular form of the chiral symmetry, these states will have a positive chirality if  $\Delta\nu$  is *negative*, and vice versa. Thus, a topological-to-trivial wall will support one zero mode, while the wall separating phases with  $\nu = \pm 1$  will support two zero modes with the same chirality.

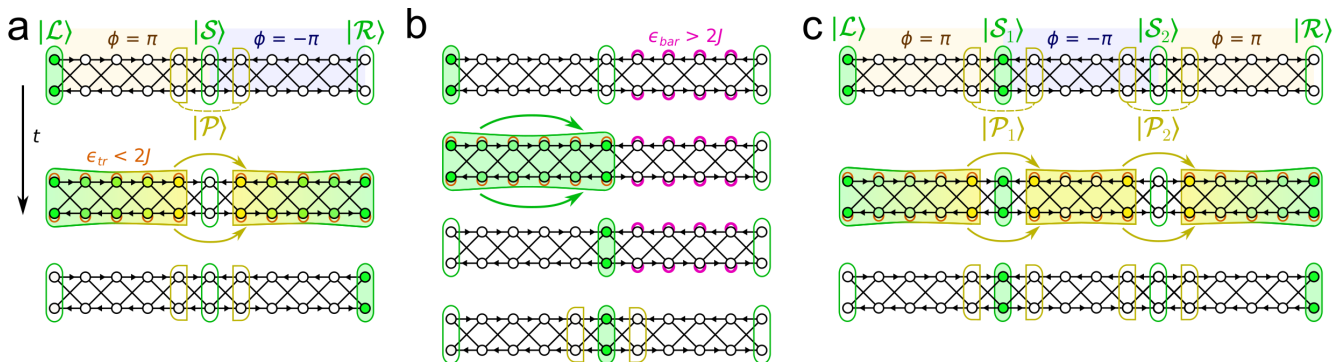


Figure 2. (a)  $\mathcal{L}$ -to- $\mathcal{R}$  transfer protocol in a two-domain Creutz ladder with  $\ell = 4$ , induced by an energy imbalance of  $\pm\epsilon_{tr}$ . One of the topological states in the domain wall,  $|\mathcal{S}\rangle$ , remains pinned at zero energy due to AB caging, while the other one,  $|\mathcal{P}\rangle$ , hybridizes with the left and right states to allow the transfer. (b)  $\mathcal{L}$ -to- $\mathcal{S}$  transfer in a two-domain ladder. The initial state, not pictured, is the same as in (a). The second domain has to be taken to the trivial phase using a control parameter of  $\epsilon_{bar} > 2J$  before inducing the transfer process. (c)  $\mathcal{L}$ -to- $\mathcal{R}$  transfer in a three-domain ladder, starting in state  $(|\mathcal{L}\rangle + |\mathcal{S}_1\rangle)/\sqrt{2}$ . The final state is  $(|\mathcal{S}_1\rangle - |\mathcal{R}\rangle)/\sqrt{2}$ . As can be seen, the transfer does not affect the intermediate  $\mathcal{S}$ -type states.

## B. Topological domains and walls

We consider a Creutz ladder with  $N$  topological domains, with their winding number taking alternate values of  $\nu = \pm 1$ . We set  $J = 1$ . Each domain will consist of two end rungs and a number  $\ell \geq 2$  of inner rungs. The length of the ladder is then  $L = N(\ell + 1) + 1$ . Each end rung, except the left- and rightmost ones, is shared between two domains, and constitutes a domain wall. This model is obtained with the following parameter scheme:

$$\phi_j = \begin{cases} \pi & \text{if } 1 \leq j \pmod{2(\ell+1)} \leq \ell+1 \\ -\pi & \text{otherwise} \end{cases} \quad (2)$$

$$\epsilon_j = \begin{cases} \epsilon_w^{(D[j])} & \text{if } j \pmod{\ell+1} = 1 \text{ (domain walls)} \\ \epsilon_b^{(D[j])} & \text{otherwise (bulk sites),} \end{cases} \quad (3)$$

where  $D[j] = \lceil (j-1)/(\ell+1) \rceil$  is the domain number to which rung  $j$  belongs, with  $\lceil \cdot \rceil$  being the ceiling function. For this purpose, we label each wall just like the domain to its left. The leftmost rung of the ladder is labeled as belonging to domain  $D[j = 1] = 0$ .

An example with  $\ell = 4$  and two domains can be seen in Fig 1 (c). A given domain  $D_0$  with a flux of  $\phi = \pm\pi$  will have a winding number of  $\nu = \pm 1$ , respectively, as long as its energy imbalance satisfies  $\epsilon_b^{(D_0)} < 2J$ . If  $\epsilon_b^{(D_0)} > 2J$ , then  $\nu = 0$  and the domain is trivial.

If we set  $\epsilon_j = 0 \forall j$  (balanced case) with the flux values defined above, the model will have left ( $|\mathcal{L}\rangle$ ) and right ( $|\mathcal{R}\rangle$ ) topological end states, as well as two topological states,  $|\mathcal{S}_k\rangle$  and  $|\mathcal{P}_k\rangle$ , in each domain wall  $k = 1, \dots, N-1$ . Given that the system presents AB caging [31, 40], all of them will be compact, i.e. localized in only a few nearby sites. An  $N$ -domain CL defined in this way has  $2N$  compact topological states pinned at exactly zero

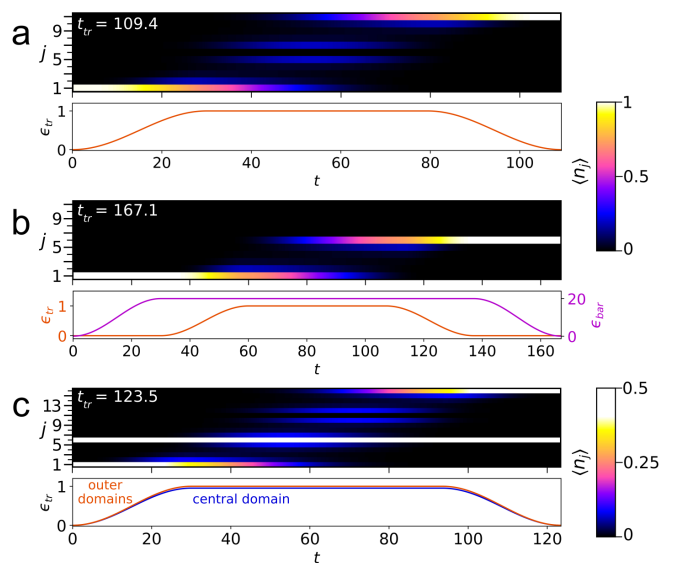


Figure 3. Numerical simulations of the processes in Fig. 2, and the control parameter pulses used. (a) Left-to-right transfer in a two-domain ladder. (b) Left-to-center transfer in a two-domain ladder. The transfer-inducing parameter  $\epsilon_{tr}$  and the barrier  $\epsilon_{bar}$  are shown on different scales. (c) Left-to-right transfer in a three-domain ladder, acting on the initial state  $(|\mathcal{L}\rangle + |\mathcal{S}_1\rangle)/\sqrt{2}$ . The component at  $|\mathcal{L}\rangle$  gets transferred, while the component at  $|\mathcal{S}_1\rangle$  remains unperturbed. The control parameter in the central domain takes a maximum value of 0.952, see main text. The rung occupation number is represented as a function of time  $t$  for each rung  $j$ . Note that different colormaps are used for subfigures (a,b) and subfigure (c). Preparation times of  $t_{prep} = t'_{prep} = 30$  are used. All times are expressed in units of  $\hbar/J$ .

energy:  $(N-1)$   $\mathcal{S}$ - and  $\mathcal{P}$ -type states, and the left and right end modes. All of them are localized in two sites, except for the  $\mathcal{P}$ -type states, which are localized in four. Their form is:

$$|\mathcal{L}\rangle = \frac{|1, A\rangle - i|1, B\rangle}{\sqrt{2}} \quad (4)$$

$$|\mathcal{R}\rangle = \frac{|L, A\rangle + (-1)^{N+1}i|L, B\rangle}{\sqrt{2}} \quad (5)$$

$$|\mathcal{S}_k\rangle = \frac{|j_k, A\rangle + (-1)^{k+1}i|j_k, B\rangle}{\sqrt{2}} \quad (6)$$

$$|\mathcal{P}_k\rangle = \frac{1}{2} [|j_k - 1, A\rangle - |j_k + 1, A\rangle + (-1)^{k+1}i(|j_k - 1, B\rangle - |j_k + 1, B\rangle)], \quad (7)$$

where  $k = 1, \dots, N - 1$ , and  $j_k = k(\ell + 1) + 1$  is the rung in which the  $k$ -th wall is located. We use  $\mathcal{S}$  and  $\mathcal{P}$  as nomenclature because their form and spatial symmetry are analogous to the  $s$  and  $p$  orbitals in an atom (or to

the two lowest levels in a quantum well in general). The four states in a two-domain ladder are represented in Fig. 1 (d), using their rung occupation number:

$$\langle n_j \rangle = \langle n_{j,A} \rangle + \langle n_{j,B} \rangle. \quad (8)$$

For reasons that will become apparent later, we will group left, right and  $\mathcal{S}$ -type states under the name of “computational states”.

We now switch on the energy imbalance for all sites except those in the domain walls without reaching the topological phase transition, that is,  $\epsilon_w^{(0)} = \epsilon_w^{(N)} = \epsilon_b^{(D)} = \epsilon_0 < 2J \forall D$ ,  $\epsilon_w^{(D)} = 0 \forall D \in [1, N - 1]$ . Then, the left, right and  $\mathcal{P}$ -type topological states will acquire a finite overlap with each other and hybridize [47] Their analytical expression before hybridization is:

$$|\mathcal{L}\rangle = -i\mathcal{N}_{\mathcal{L}} \sum_{j=1}^{\ell+1} \left(\frac{2iJ}{\epsilon}\right)^{-j} |j\rangle \otimes \begin{pmatrix} 1 \\ -i \end{pmatrix} \quad (9)$$

$$|\mathcal{R}\rangle = (-1)^{N+1}i\mathcal{N}_{\mathcal{R}} \sum_{j=L-\ell}^L \left((-1)^N \frac{2iJ}{\epsilon}\right)^{j-L-1} |j\rangle \otimes \begin{pmatrix} 1 \\ (-1)^{N+1}i \end{pmatrix} \quad (10)$$

$$|\mathcal{P}_k\rangle = (-1)^{k+1}i\mathcal{N}_{\mathcal{P}_k} \left[ \sum_{j=(k-1)(\ell+1)+2}^{k(\ell+1)} \left((-1)^k \frac{2iJ}{\epsilon}\right)^{j-k(\ell+1)-1} |j\rangle \otimes \begin{pmatrix} 1 \\ (-1)^{k+1}i \end{pmatrix} - \sum_{j=k(\ell+1)+2}^{(k+1)(\ell+1)} \left((-1)^k \frac{2iJ}{\epsilon}\right)^{k(\ell+1)-j+1} |j\rangle \otimes \begin{pmatrix} 1 \\ (-1)^{k+1}i \end{pmatrix} \right], \quad (11)$$

where  $\mathcal{N}_{\mathcal{L}, \mathcal{R}, \mathcal{P}}$  are normalization constants, and can be approximated with a very small margin of error for  $\ell \gtrsim 3$  as:

$$\mathcal{N}_{\mathcal{L}} = \mathcal{N}_{\mathcal{R}} \approx \sqrt{\frac{4J^2/\epsilon^2 - 1}{2}} \quad (12)$$

$$\mathcal{N}_{\mathcal{P}} \approx \frac{1}{\sqrt{2}} \left( \frac{1}{4J^2/\epsilon_l^2 - 1} + \frac{1}{4J^2/\epsilon_r^2 - 1} \right)^{-1/2}, \quad (13)$$

where  $2\epsilon_{l,r}$  are the values of the energy imbalance in the domains to the left and right of the relevant domain wall. The gauge was chosen to coincide with Eqs. (4-7).

Given that all domain walls are still balanced (i.e. both their on-site energies remain at zero), all  $\mathcal{S}$ -type states will remain localized on the two sites, due to magnetic interference. This is pictured in Fig. 1 (e) for a two-domain ladder, where bonding and antibonding states appear, with the form  $|\pm\rangle = (|\mathcal{L}\rangle - |\mathcal{R}\rangle)/2 \pm i^\ell |\mathcal{P}\rangle/\sqrt{2}$ , as well as a dark state at zero energy,  $|0_{\mathcal{LR}}\rangle = (|\mathcal{L}\rangle + |\mathcal{R}\rangle)/\sqrt{2}$ .

Each state is confined to the domains adjacent to its domain wall, or to the first (last) domain in case of the left (right) end states. All states have the same exponential profile, which is analogous to the Majorana bound states in the Kitaev chain, as derived in [48, 49] for the balanced CL. The states deviate slightly from these expressions for very short domain lengths and values of  $\epsilon$  close to the topological phase transition, due to finite size effects ( $\delta_{\mathcal{L}} = \left\| |\mathcal{L}\rangle_{\text{num}} - |\mathcal{L}\rangle_{\text{analyt}} \right\| = 0.16$  for  $\ell = 2$  and  $\epsilon = 1.5J$ ), but are remarkably accurate otherwise ( $\delta_{\mathcal{L}} = 0.016$  for  $\ell = 4$  and  $\epsilon = J$ ).

### C. Effective Hamiltonian

Using these analytical expressions, we can obtain an effective Hamiltonian for the topological states in an  $N$ -domain imbalanced CL with  $\epsilon = 0$  in its walls:

$$\mathcal{H}_{\text{eff}} = v_1 |\mathcal{P}_1\rangle\langle\mathcal{L}| + v_N |\mathcal{R}\rangle\langle\mathcal{P}_{N-1}| + \sum_{k=2}^{N-1} v_k |\mathcal{P}_k\rangle\langle\mathcal{P}_{k-1}| + h.c., \quad (14)$$

where  $v_1 = \langle\mathcal{P}_1|\mathcal{H}|\mathcal{L}\rangle$ ,  $v_k = \langle\mathcal{P}_k|\mathcal{H}|\mathcal{P}_{k-1}\rangle$  for  $k = 2, \dots, N-1$ , and  $v_N = \langle\mathcal{R}|\mathcal{H}|\mathcal{P}_{N-1}\rangle$ .

It takes the form of a 1D chain of length  $N+1$ , with only nearest-neighbour hopping amplitudes. Each of the  $\mathcal{S}$ -type states is completely decoupled, and so they do not appear in the Hamiltonian.

Using expressions (9-11), we obtain the following expression for the hopping amplitudes:

$$v_k = 2(-1)^{d+p_{k-1}} \epsilon \mathcal{N}_k \mathcal{N}_{k-1} \left[ (-1)^k \frac{2iJ}{\epsilon} \right]^{-d-2}, \quad (15)$$

where  $\mathcal{N}_k, \mathcal{N}_{k-1}$  are the normalization constant for the involved states and  $d$  is the distance between the maxima between topological states numbers  $k-1$  and  $k$ , with  $|\mathcal{L}\rangle$  being the zeroth state and  $|\mathcal{R}\rangle$  being the  $N$ -th. The distance is  $d = \ell - 1$  between two  $\mathcal{P}$  states,  $d = \ell$  between an end state and a  $\mathcal{P}$  state, and  $d = \ell + 1$  between the two end states in a single-domain ladder.  $p_{k-1} = 0$  if the  $(k-1)$ -th state is a  $\mathcal{P}$  state, and  $p_{k-1} = 1$  otherwise.

Using this effective Hamiltonian, it is easy to understand the dynamics of the topological states. If the system is initialized in state  $|\mathcal{L}\rangle$ , time evolution will eventually take it to state  $|\mathcal{R}\rangle$ , using each  $\mathcal{P}$ -type state of the ladder as a way to leapfrog its domain wall without affecting its  $\mathcal{S}$ -type state. The values of the energy imbalance in each domain can be tuned in order to implement a transfer protocol between the two end states.

We have used this effective Hamiltonian to estimate transfer times and parameter values, but all numerical results have been obtained solving the full model.

#### D. Controlled transfer protocol

In order to start and stop the transfer when desired without disrupting the dynamics, the control parameter of the system, the energy imbalance, must be turned on and off in a smooth way. To this end, we employ a control pulse with three parts: first, we increase the control parameter in a sinusoidal manner; then, we keep the parameter constant for some time, and finally, the parameter returns to zero, also in a sinusoidal way. In domain  $D$ , this pulse has the form:

$$\epsilon_{\text{tr}}^{(D)}(t) = \begin{cases} \epsilon_{\text{tr}}^{(D)} \sin^2(\Omega t) & \text{for } 0 < t < t_{\text{prep}} \\ \epsilon_{\text{tr}}^{(D)} & \text{for } t_{\text{prep}} < t < t_{\text{tr}} - t_{\text{prep}} \\ \epsilon_{\text{tr}}^{(D)} \sin^2[\Omega(t - t_{\text{tr}})] & \text{for } t_{\text{tr}} - t_{\text{prep}} < t < t_{\text{tr}}, \end{cases} \quad (16)$$

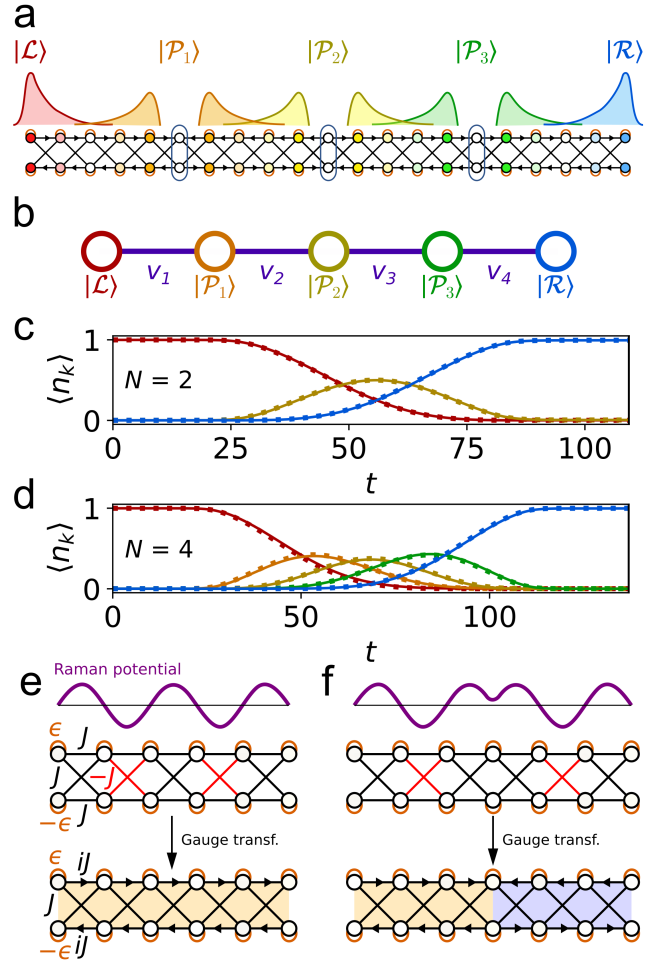


Figure 4. (a) Topological states involved in an LR transfer in a four-domain Creutz ladder. (b) Associated effective model, corresponding to a 1D chain. (c) Occupation of the topological states during an LR transfer in a two-domain ladder with  $\ell = 4$  ( $L = 11$ ), where the only  $\mathcal{P}$  state is represented in yellow. Numerical results for the full Creutz ladder Hamiltonian are pictured in continuous line, while the analytical prediction by the effective Hamiltonian is plotted in dotted lines. This process is also pictured in Fig. 3 (a). (d) Occupation of the topological states in an LR transfer in the four-domain ladder pictured in (a), with  $\ell = 4$  ( $L = 21$ ). (e) Effective model for the cold atoms system in [22], corresponding to a single-domain CL. (f) Setup for a two-domain CL. The corresponding Raman potentials are pictured in purple. All hopping amplitudes have an additional minus sign.

where  $t_{\text{tr}}$  is the total transfer time. We allow the maximum value of the pulse to be different for each domain, but always consider mirror-symmetric distributions (i.e.  $\epsilon_{\text{tr}}^{(D)} = \epsilon_{\text{tr}}^{(N-D+2)}$ ). All times are expressed in units of  $\hbar/J$ , and we take  $\hbar = 1$ . The preparation time  $t_{\text{prep}} = \pi/(2\Omega)$  must be sufficiently large (numerical results suggest  $t_{\text{prep}} \gtrsim 20/J$ ) so that the Hamiltonian changes adiabatically and the particle remains in the subspace of computational states, with the same components as in the initial configuration. We consider this

type of pulse, already used in the literature [50], because it provides smooth initial and final preparation stages, but also includes a period where the control parameter is constant, therefore simplifying its implementation.

The fidelity threshold required for the final state in all transfer simulations of the paper is taken to be  $f_0 = 0.995$ , well above the current estimations of quantum error correction thresholds, which are around 0.99 [51–54].

We can see a scheme of this process in Fig. 2 (a,c) for two and three-domain ladders, respectively. In Fig. 2 (c), state  $(|\mathcal{L}\rangle + |\mathcal{S}_1\rangle)/\sqrt{2}$  (which can itself be prepared using transfer operations) evolves to  $(-|\mathcal{R}\rangle + |\mathcal{S}_1\rangle)/\sqrt{2}$ , demonstrating that the  $\mathcal{S}$ -type states located between the origin and destination of the transfer are unaffected by it. Numerical simulations of these processes are shown in Fig. 3 (a,c) for  $\ell = 4, J = 1, t_{\text{prep}} = 30$ . Case (a) has  $\epsilon_{\text{tr}}^{(1)} = \epsilon_{\text{tr}}^{(2)} = 1$ .

Using the effective Hamiltonian it was found that, in general, the transfers with  $N > 2$  have to be implemented using a different value of  $\epsilon_{\text{tr}}^{(D)} = \epsilon_{\text{tr}}^{(N-D+2)}$  for each pair of domains related by mirror symmetry, in order to achieve a fidelity greater than  $f_0$ . For example, the three-domain protocol in Fig. 2 (c) uses  $\epsilon_{\text{tr}}^{(1)} = \epsilon_{\text{tr}}^{(3)} = 1$  and  $\epsilon_{\text{tr}}^{(2)} = 0.952$ . The different values of  $\epsilon_{\text{tr}}^{(D)}$  for all protocols, as well as further explanation on this point, are provided in Appendix B. The use of different control pulses in different domains can provide an exponential speed-up in cases with large  $L$ , as we explore in Section III.

More complex protocols acting on the topological states can also be considered, and will be explored in future works.

Finally, to demonstrate the accuracy of the effective Hamiltonian, transfers between the left and right end modes (which we will call *left-to-right* or *LR transfers*) were simulated in two- and four-domain ladders with  $\ell = 4$ , and then compared to the results predicted by the

effective model. The topological state occupation  $\langle n_k \rangle$  is shown in Fig. 4 at each time  $t$ , with  $\langle n_0 \rangle = |\langle \mathcal{L} | \psi(t) \rangle|^2$ ,  $\langle n_k \rangle = |\langle \mathcal{P}_k | \psi(t) \rangle|^2$  for  $1 < k < N - 1$ , and  $\langle n_N \rangle = |\langle \mathcal{R} | \psi(t) \rangle|^2$ . As can be seen, both results are almost identical.

In this work, we choose an energy imbalance as a control parameter, but analogous protocols can be implemented introducing a vertical hopping amplitude between the legs instead, with a Hamiltonian term of the form  $\mathcal{H}_m = -\sum_{j=1}^L (mc_{j,A}^\dagger c_{j,B} + h.c.)$ . In most experimental implementations, this alternative is more difficult to implement, and its protection against disorder is equivalent to the imbalanced case, but we include a discussion on this version of the models in Appendix C for completeness, including their different symmetry classes.

### E. Transfers involving $\mathcal{S}$ -type states

The same kind of transfer can also be implemented with the  $\mathcal{S}$ -type states, with some additional steps. To swap the components of, for instance, states  $|\mathcal{L}\rangle$  and  $|\mathcal{S}_k\rangle$ , the first step is to turn the  $k$ -th domain wall into a topological-to-trivial wall. This is achieved by raising the value of  $\epsilon$  in the domain immediately to its right ( $D = k + 1$ ), to a sufficiently high value so that the domain becomes trivial,  $\epsilon_{k+1}^{(b)} = \epsilon_{\text{bar}} > 2J$ , taking a time  $t'_{\text{prep}}$ . This makes state  $|\mathcal{P}_k\rangle$  disappear without affecting  $|\mathcal{S}_k\rangle$ , and acts like a barrier for the spread of the computational states. A large value of the barrier,  $\epsilon_{\text{bar}} \gtrsim 20\epsilon_{\text{tr}}$ , has been observed to be more effective in this task.

Then, just like in the LR transfer, the energy imbalance in all intermediate bulk sites has to be switched on (now including domain wall  $k$ ), while leaving the intermediate domain walls at zero energy. The  $\mathcal{S}$  state will then take an exponential profile into the domain to its right (or left, if the barrier was set up to its right):

$$|\mathcal{S}_k\rangle_{\text{left}} = (-1)^{k+1} i \mathcal{N}_{\mathcal{S}_k} \sum_{j=(k-1)(\ell+1)+2}^{k(\ell+1)} \left( (-1)^k \frac{2iJ}{\epsilon} \right)^{j-k(\ell+1)-1} |j\rangle \otimes \begin{pmatrix} 1 \\ (-1)^{k+1} \end{pmatrix}_i \quad (17)$$

$$|\mathcal{S}_k\rangle_{\text{right}} = (-1)^{k+1} i \mathcal{N}_{\mathcal{S}_k} \sum_{j=k(\ell+1)+2}^{(k+1)(\ell+1)} \left( (-1)^k \frac{2iJ}{\epsilon} \right)^{k(\ell+1)-j+1} |j\rangle \otimes \begin{pmatrix} 1 \\ (-1)^{k+1} \end{pmatrix}_i, \quad (18)$$

where the subindex indicates the side into which the state extends.

The process is schematized for a two-domain ladder in Fig. 2 (b), and simulated in Fig. 3 (b) for  $\ell = 4, J = 1, \epsilon_{\text{tr}} = 1, \epsilon_{\text{bar}} = 20J, t_{\text{prep}} = t'_{\text{prep}} = 30$ . Instead of inducing trivial domains, an alternative that may be easier to implement in some platforms would be to completely disconnect the rest of the system, by switching off the

appropriate hopping amplitudes.

Using the described protocols, the occupation of any two computational states in a multidomain CL (left, right or  $\mathcal{S}$ -type) can be swapped. This makes it a suitable model for the implementation of quantum information tasks such as remote quantum gates, braiding or entanglement generation in photonic lattices or superconducting circuits, which will be the subject of future work.

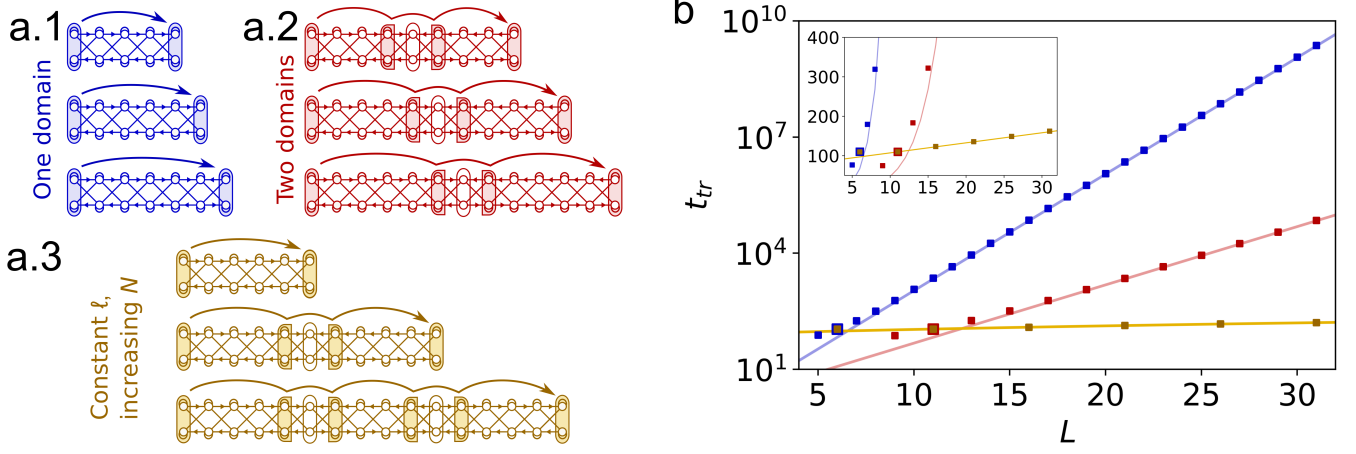


Figure 5. Transfer time between left and right states in a Creutz ladder as a function of distance. (a) The three cases considered are (a.1) a single domain of increasing length, in blue, (a.2) two domains of increasing length, with a single amplifier between them, in red, and (a.3) an increasing number of domains of length  $\ell = 4$ , in yellow. (b) Transfer time  $t_{tr}$  in the three cases as a function of the total length of the ladder  $L$ , color coded as in (a). A logarithmic scale is used for the vertical axis. The first and second yellow points coincide with a blue point and a red point, respectively. The simulations have a maximum control parameter of  $= 1$ , a preparation time of  $t_{\text{prep}} = 30$ , and a time step of  $\Delta t = 0.1$ . Analytical results for the transfer times [Eqs. (20,21)] are included in continuous red and blue lines. A linear fit is plotted for the yellow points. In the inset, the same data is plotted using a linear vertical scale, in order to appreciate the different trends of the data.

Given that our model is a quasi-1D platform with full connectivity between its nodes, it can be used as a basic element in a more complex 2D or 3D structure, in order to achieve a quantum processor with a really high connectivity.

### F. Acquired phase

A complex phase is acquired in general by the transferred components of the wavefunction. This phase factor can be easily obtained using the effective model, and depends on the domain length  $\ell$ , the direction of transfer and the chirality of the states involved, and is given by:

$$\zeta(\ell, n_w, x, \varsigma) = \begin{cases} (-1)^{n_w/2 + \delta_{x,\varsigma}} [(-1)^{\delta_{x,\varsigma} i}]^\ell & \text{for even } n_w \\ (-1)^{(n_w-1)/2} & \text{for odd } n_w, \end{cases} \quad (19)$$

where  $n_w$  is the number of domain walls between the transferred states,  $x = \pm 1$  is the chirality of the leftmost transferred state (e.g.,  $x = -1$  if state  $|\mathcal{L}\rangle$  is involved), and  $\varsigma = 1(-1)$  indicates the direction of transfer, from left to right (from right to left) [55]. The two latter quantities are then compared in a Kronecker delta  $\delta_{x,\varsigma}$ .

This formula does not depend on  $\ell$  for odd  $n_w$ , due to the way the end modes hybridize. The expression assumes the gauge chosen in Eqs. (4-7), and its form is related to the presence or absence of reflection and inversion symmetries in each case. The acquired phase, in any case, can only be a multiple of  $\pi/2$ , and it is remarkably robust against disorder (even symmetry-breaking disorder),

as is usually the case in topological protocols. This is further discussed in Appendix D.

### G. Experimental proposal

As mentioned in the introduction, the imbalanced Creutz ladder can be implemented using state-of-the-art technology in ultracold atoms [22–24, 31], superconducting circuits [25, 26] and photonic lattices [27], in both waveguide and cavity arrays. For our protocols, it is crucial that the energy imbalances can be tuned individually, something that can be easily done in most implementations. Additionally, the Peierls phases from the synthetic magnetic field must be able to change sign from one cell to the next in order to implement a domain wall with a width of a single rung. This is attainable in the photonic and circuit QED implementations, given that the Peierls phases are obtained with an on-site energy driving, which can be modified to separately choose the phase of each bond. On the other hand, the ultracold atoms setup in [24] might be able to engineer a multidomain ladder if a more complex pattern of standing waves is used, where the resulting Peierls phase depends on position.

However, the tight-binding model implemented with fermionic atoms in [22], with spin acting as a synthetic dimension to create the two rungs, is especially suited to implement multidomain Creutz ladders. The tight-binding model that the authors present in said work is related to the usual Creutz ladder model by the gauge transformation  $c_{j,\sigma} \rightarrow \exp[i\pi s_\sigma(3/2 - j)/2]c_{j,\sigma}$ , with  $s_\sigma = \delta_{\sigma,A} - \delta_{\sigma,B}$ , which only affects the relative phases

between wavefunction components, but not the relevant physical results. This can be easily seen by examining the magnetic flux for each closed loop in both lattices, and realizing they are identical.

The authors build this model using a staggered Raman coupling with positive and negative terms, which induces a pseudo-spin-orbit term that creates the diagonal links [see Fig. 4 (e)]. Under this gauge transformation, a system where all even (odd) unit cells have a negative Raman coupling term corresponds to the  $\nu = 1$  ( $-1$ ) phase of the Creutz ladder. Thus, the Raman potential can be modified to create different domains by setting up regions with different alternating patterns of signs [56], as shown in Fig. 4 (f). The appearance of flat bands requires the horizontal and diagonal hopping amplitudes to be equal in magnitude. A promising aspect of this setup is that the use of a synthetic dimension will cause noise-induced fluctuations in the different links of each unit cell to be highly correlated, which is the kind of disorder which does not break the protecting chiral symmetry, as we explain in Section III B and Appendix C.

### III. FAST LONG-RANGE TRANSFER

#### A. Topological domain walls as amplifiers

In all protocols based on the hybridization of end modes in 1D topological insulators, the transfer time increases exponentially with distance for a fixed control parameter value [57]. This is because the exponential localization of the modes causes their overlap –and bonding energy– to shrink exponentially as the distance between them increases. This causes the transfer dynamics to be extremely slow in large systems.

However, there is a workaround that can help us with this issue. Using the effective Hamiltonian, we obtain the left-to-right transfer times for the single- and two-domain CL:

$$t_{tr}^{(N=1)} = \frac{\pi\epsilon}{2(4J^2 - \epsilon^2)} \left(\frac{2J}{\epsilon}\right)^{\ell+3} = \frac{\pi\epsilon}{2(4J^2 - \epsilon^2)} \left(\frac{2J}{\epsilon}\right)^{L+1} \quad (20)$$

$$t_{tr}^{(N=2)} = \frac{\pi\epsilon}{4J^2 - \epsilon^2} \left(\frac{2J}{\epsilon}\right)^{\ell+2} = \frac{\pi\epsilon}{4J^2 - \epsilon^2} \left(\frac{2J}{\epsilon}\right)^{(L+1)/2}. \quad (21)$$

This expression does not take into account the preparation time, which soon becomes negligible as the transfer times increase. Even though both times grow exponentially with the transfer distance  $L$ , the presence of an intermediate  $\mathcal{P}$  state in the two-domain ladder dramatically speeds up the transfer, halving the coefficient in the exponent. The  $\mathcal{P}$  state works as a signal booster or amplifier that increases the effective hopping amplitude between the left and right end states. The exponential dependence turns out to depend only on domain length

$\ell$ , so we can lose the exponential behaviour altogether by using a constant value of  $\ell$  for ladders of growing length, simply by increasing the number of domains.

We demonstrate this in Fig. 5, in which we plot the transfer time as a function of distance for the single- and two-domain cases, as well as for a ladder of increasing  $N$  but fixed  $\ell$ . We include both numerical and analytical results for one and two domains, which are remarkably accurate for large systems. We set  $\epsilon_{tr}^{(1)} = J, t_{\text{prep}} = 30$ , and a time step of  $\Delta t = 0.1$  for all simulations. A domain length  $\ell$  similar to the localization length of the topological states during the transfer,  $\lambda(\epsilon_{tr}) = 1/\log(2J/\epsilon_{tr})$  [obtained from Eqs. (9-11)], must be chosen, in order for the amplification to be effective. We use  $\ell = 4$  for the multidomain simulations with  $\epsilon_{tr}^{(1)} = J$ , given that the localization length is then  $\lambda = 3.32$ .

The transfer times with constant  $\ell$  can be fitted to a linear function  $t_{tr} = t_0 + A_0 L$ , with  $t_0 = 81.66$  and  $A_0 = 2.55$ . The first point was not included in the fit. The optimal maximum values for the control parameter in simulations with  $N > 2$  were obtained numerically using the effective Hamiltonian, and are included in Table I, inside Appendix B.

The concern may arise that this could also make the protocols more fragile against noise. However, as we show in the following section, the topological protection of these protocols show the expected plateau at  $f = 1$  for low disorder levels when the corresponding chiral symmetry is preserved, and when it is not, their shortened times actually make them much more robust than the single-domain case.

The notion of topological amplification in non-Hermitian models (i.e. using topological states to exponentially amplify a signal) has been recently explored in the literature [58–63]. In some aspects, the protocols we propose in our work are similar in spirit to this idea: both cases involve amplifying a signal (in our case, the wavefunction of the states involved in the transfer) by coupling it to the low-amplitude end of an exponentially localized topological state. However, the nature of the amplification and the topological protection in these works are different, given their non-Hermitian Hamiltonians with intrinsic symmetries, robust to all kinds of disorder while valid.

#### B. Robustness against disorder

In this section, we study the effects of disorder on the LR transfer protocols defined above using their fidelity, which is defined as  $f = |\langle \mathcal{R} | \psi(t_{tr}) \rangle|^2$ , where  $|\psi(t_{tr})\rangle$  is the state obtained at the end of the protocol. We consider the standard, single-domain case, and also the case with four domains. In order to identify the effects of topological protection, we also consider two trivial transfer protocols, one using a 1D chain of sites with hopping amplitude  $J$ , and the other using a Creutz ladder with no magnetic flux ( $\phi = 0$ ). These protocols involve tuning the chemical



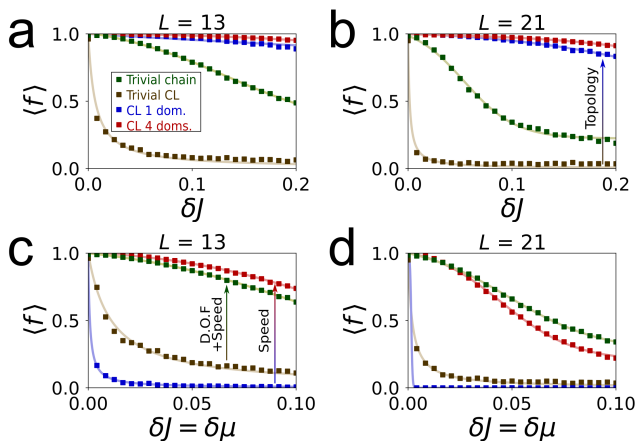


Figure 6. Fidelity of the transfer protocols against quenched disorder. We compare trivial transfer protocols in a 1D chain and in a Creutz ladder to the single- and four-domain topological CL protocols, for a fixed length  $L$ . We study the cases  $L = 13, 21$ . We consider both off-diagonal disorder which only depends on  $j$  (a,b) and general uncorrelated disorder, both diagonal and off-diagonal (c,d), see main text. The effect of topological protection can be seen in (a,b), where the topological protocols show a plateau for low values of disorder. Note the different horizontal scale for (a,b) and (c,d). In the case with symmetry-breaking disorder, the multidomain protocol performs much better than the single-domain one, due to its shorter transfer time. It is comparable with the fidelity of the trivial chain protocol, which has a much smaller amount of degrees of freedom that can be affected by disorder. Sigmoid functions fitted to the data are provided as a guide for the eye. Transfer times for  $L = 13$  are  $t_{\text{tr}} = 332.3, 3567.7, 9013.8, 63.0$  for the trivial chain, the trivial CL and the single- and four-domain CL, respectively. In the same order, the times for  $L = 21$  are  $t_{\text{tr}} = 800.5, 46739.8, 2288679.9, 135.5$ .

potential of the end sites of the models, starting at a low value  $-\mu_0$  to create two potential wells on either side, and then adiabatically increasing its value up to zero during a preparation time  $t_{\text{prep}}$ . The potential wells are then re-established adiabatically, by lowering the potentials down to  $-\mu_0$  again. We consider a fixed value of  $\mu_0 = 10J = 10$  and  $t_{\text{prep}} = t_{\text{tr}}/2$ , and then find the optimal transfer time in the ideal system that satisfies  $f > 0.985$  (for the trivial chain) or  $f > 0.95$  (for the Creutz ladder).

We consider quenched disorder in the timescale of the protocols (i.e. constant in time for each realization). It is important to note that we do not calibrate the transfer time for each realization, given that this would often not be feasible in a real system. We study two disorder regimes: off-diagonal disorder, which preserves the chiral symmetry of the CL, and a case with both diagonal and off-diagonal disorder, which breaks it. In the former case, we consider fluctuations which only depend on the longitudinal coordinate of the ladder  $j$ , in order to preserve the chiral symmetry of the ladder  $\mathcal{X}_C$  (see Appendix C):

$$\begin{cases} -J_{j,\sigma}^{(h)} &= -|J + \delta J R_j| e^{i\phi/2} \\ -J_{j,\sigma}^{(d)} &= -|J + \delta J R_j|, \end{cases} \quad (22)$$

where  $\delta J$  is the level of off-diagonal disorder,  $-J_{j,\sigma}^{(h)}$  and  $-J_{j,\sigma}^{(d)}$  are the horizontal and diagonal hopping terms connecting site  $j, \sigma$  to the sites on its right, and  $R_j$  are random numbers in the interval  $[-0.5, 0.5]$ .

For the case with general disorder, we consider the following fluctuations:

$$\mu_{j,\sigma} = s_\sigma \epsilon + \delta \mu R_{j,\sigma}^{(\mu)} \quad (23)$$

$$\begin{cases} -J_{j,\sigma}^{(h)} &= -|J + \delta J R_{j,\sigma}^{(h)}| e^{i\phi/2} \\ -J_{j,\sigma}^{(d)} &= -|J + \delta J R_{j,\sigma}^{(d)}| \end{cases}, \quad (24)$$

where  $\delta \mu$  and  $\delta J$  represent the level of diagonal and off-diagonal disorder respectively,  $\mu_{j,\sigma}$  is the total on-site potential on site  $j, \sigma$ , and all different  $R$  variables are independent random numbers in the interval  $[-0.5, 0.5]$ , and are now uncorrelated for all different sites and bonds.

As we explain in Appendix C, fluctuations in the control parameters  $\epsilon_j$  do not break the chiral symmetry if they are equal for both sites in each rung, something crucial for the robustness of the protocol.

We display the results in Fig. 6 for systems of length  $L = 13, 21$ . As can be seen in Fig. 6 (a,b), the topological protocols show a plateau at low disorder strength as long as the chiral symmetry is preserved. In the case with general disorder [Fig. 6 (c,d)], the four-domain case performs considerably better than the single-domain case, due to its decreased transfer time. Its fidelity is then similar to the trivial chain case, even though the latter has a much smaller number of degrees of freedom that can fluctuate. The complexity of the model and the increased transfer time also explain the worse performance of the trivial CL when compared to the chain. We include a detailed description of the different factors that we observed that can affect the robustness of the studied protocols in Appendix D.

The acquired phase in the transfer is, however, much more robust in the topological case than in the trivial chain. This can be useful for quantum information applications of these protocols, for example in photon-mediated remote gates [7] or superconducting qubit implementations [10]. We elaborate on this point in Appendix D, and showcase its usefulness in a simple case involving the transfer of two superposed states.

#### IV. AMPLIFIERS IN THE SSH CHAIN

The question arises whether these transfer protocols can work in simpler topological models, like for example the SSH chain. Although this model only possesses

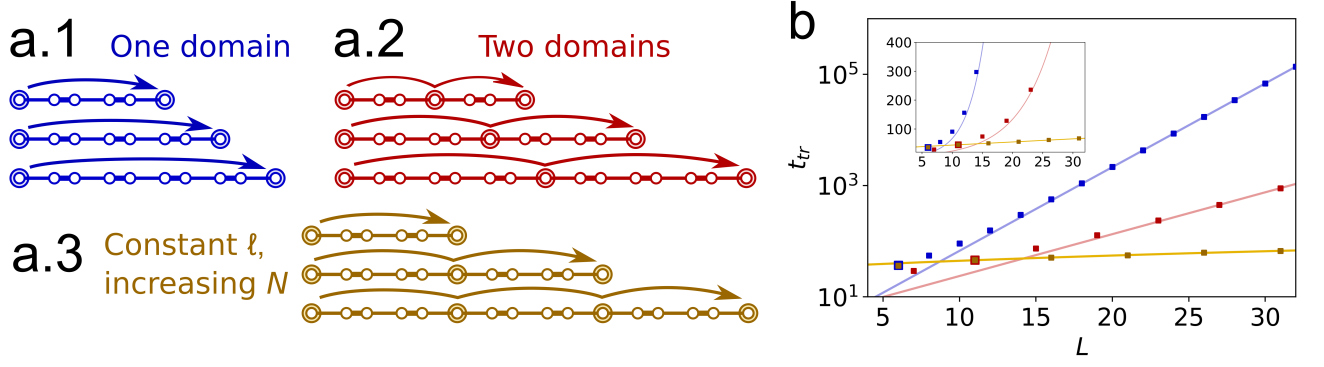


Figure 7. Transfer time between left and right states in an SSH chain as a function of distance. (a) We consider (a.1) a single domain of increasing length, in blue, (a.2) two domains of increasing length, in red, and (a.3) an increasing number of domains of length  $\ell = 4$ , in yellow. (b) Transfer time  $t_{tr}$  in the three cases as a function of the total length of the chain  $L$ , color coded as in (a). A logarithmic scale is used for the vertical axis. The first and second yellow points coincide with a blue point and a red point, respectively. The simulations have a maximum control parameter of  $v_{tr} = 0.5$ , a preparation time of  $t_{prep} = 15$ , and a time step of  $\Delta t = 0.1$ . Analytical results for the transfer times [Eqs. (27,28)] are included in continuous red and blue lines. A linear fit is plotted for the yellow points. In the inset, the same data is plotted using a linear scale, in order to appreciate the different trends of the data.

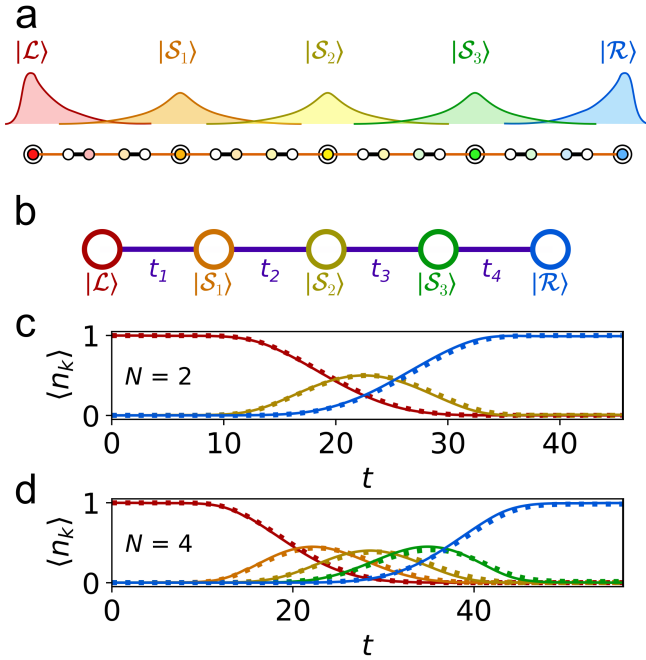


Figure 8. (a) Topological states involved in an LR transfer in a four-domain SSH chain. (b) Associated 1D effective model. (c) Occupation of the topological states during an LR transfer in a two-domain SSH chain with domain length  $\ell = 4$  ( $L = 11$ ), where the only  $\mathcal{S}$  state is represented in yellow. Numerical results for the full SSH chain Hamiltonian are pictured in continuous lines, while the analytical prediction by the effective Hamiltonian is plotted in dotted lines. (d) Occupation of the topological states in an LR transfer in the four-domain SSH chain pictured in (a), with  $\ell = 4$  ( $L = 21$ ).

a trivial and a topological phase, different topologically nontrivial domains can be established due to its particular chiral basis, where the end of a topological system can be made trivial by removing a site or vice versa. This allows us to create topological domain walls in SSH chains by simply removing a site (or, equivalently, setting up two contiguous spatial regions with the two different dimerizations). This is a well-known even-odd effect that has been studied since the conception of the SSH model [41].

The Hamiltonian that describes an SSH chain with  $N$  such domains is:

$$\mathcal{H}_{SSH} = - \sum_{k=1}^N \left\{ \delta_{1, k \bmod 2} \sum_{x=x_k^i}^{x_k^f} \left( v_k c_{x,b}^\dagger c_{x,a} + w c_{x+1,a}^\dagger c_{x,b} + h.c. \right) + \delta_{0, k \bmod 2} \sum_{x=x_k^i}^{x_k^f} \left( v_k c_{x-1,b}^\dagger c_{x,a} + w c_{x,a}^\dagger c_{x,b} + h.c. \right) \right\}, \quad (25)$$

where  $x_k^i = \lceil ((k-1)(\ell+1)/2) \rceil + 1$  (resp.  $x_k^f = \lceil k(\ell+1)/2 \rceil$ ) is the first (resp. last) unit cell that the  $k$ -th domain has support on,  $\ell$  is the number of inner sites in a domain,  $w$  takes a fixed value and  $v_k$  are the control parameters for each domain, and  $\delta_{x,y}$  are Kronecker deltas. The first term is nonzero for odd domains, and the second one, for even ones. Operator  $c_{x,\alpha}^{(\dagger)}$  destroys (creates) a particle in unit cell  $x = 1, \dots, \lceil L/2 \rceil$  and sublattice  $\alpha = a, b$ .  $L = N(\ell+1) + 1$  is the total length of the chain. We will restrict our study to the case with even  $\ell$ , given that then, all boundary states are localized in a single site in the compact limit. We also consider  $w = 1$ .

Each of the  $N-1$  domain walls holds a single state  $|\mathcal{S}_k\rangle$ , which makes a total of  $N+2$  protected boundary states, counting the left and right end states. By manipulating the control parameters  $v_k$  in the same way as the energy imbalance in the Creutz ladder, the transfer protocols we propose can be established between the left and right end modes. Now, the compact states limit corresponds to the completely dimerized chain, in which the first and last sites are completely decoupled from the rest. The acquired phases are now:

$$\zeta(\ell, n_w) = \begin{cases} (-1)^{(n_w+\ell)/2} & \text{for even } n_w \\ (-1)^{(n_w+1)/2} i & \text{for odd } n_w, \end{cases} \quad (26)$$

where  $n_w$  is the number of domain walls between the transferred states.

The absence of  $\mathcal{P}$ -type states implies that processes like the one depicted in Fig. 3 (c), where an intermediate state is unperturbed by a transfer happening through it, are impossible. However, the domain wall states can still be used as amplifiers between the left and the right end states, also achieving an exponential speedup with respect to the single-domain case, as shown in Fig. 7 for  $v_{\text{tr}} = 0.5$ . All protocol parameters are shown in Appendix B.

The transfer times for single- and two-domain models can be analytically obtained with the appropriate effective Hamiltonian, which is also derived in [42]. Its details are included in Appendix E. These transfer times are:

$$t_{\text{tr}}^{(N=1)} = \frac{\pi v}{2(w^2 - v^2)} \left(\frac{w}{v}\right)^{\ell/2+2} = \frac{\pi v}{2(w^2 - v^2)} \left(\frac{w}{v}\right)^{L/2+1} \quad (27)$$

$$\begin{aligned} t_{\text{tr}}^{(N=2)} &= \frac{\pi\sqrt{w^2 + v^2}}{\sqrt{2}(w^2 - v^2)} \left(\frac{w}{v}\right)^{\ell/2+1} \\ &= \frac{\pi\sqrt{w^2 + v^2}}{\sqrt{2}(w^2 - v^2)} \left(\frac{w}{v}\right)^{(L+1)/4} \end{aligned} \quad (28)$$

In Fig. 8, we show a four-domain SSH chain with  $\ell = 4$  (a) and the associated effective model (b). We also show the evolution of the boundary states occupation, both exactly and using the effective model, in an LR transfer in a two-domain (c) and in a four-domain (d) SSH chain, both with  $\ell = 4, v_{\text{tr}} = 0.5$ .

Finally, we studied the behaviour against off-diagonal and general (both off-diagonal and diagonal) disorder. The results can be seen in Fig. 9 for systems of length 13 and 21 (or, in the case of the single-domain SSH chain, which always has an even number of sites,  $L = 12$  and 20). In the SSH chain, the chiral symmetry is preserved for all possible off-diagonal disorder terms, and so the topological protocols show a plateau in their fidelity results for disorder levels up to more than  $0.2J$ . In the case of general disorder, the four-domain chain also shows an

almost perfect performance up to at least  $0.1J$ , showing a clear advantage over the single-domain and the trivial one, due to its much shorter transfer time.

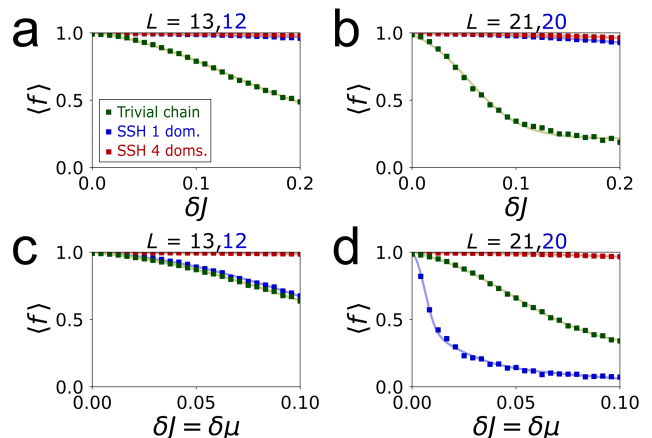


Figure 9. Fidelity of the SSH chain transfer protocols against quenched disorder. We compare a transfer protocol in a trivial chain to the single- and four-domain topological SSH chain protocols, for a fixed length  $L$ . We study the cases  $L = 13, 21$ , except in the single-domain SSH chain, where the total length has to be even, so we choose  $L = 12, 20$ . We consider off-diagonal disorder (a,b) and both diagonal and off-diagonal disorder at the same time (c,d), see main text. The effect of topological protection can be seen in (a,b), where the topological protocols show a plateau for low values of disorder. Note the different horizontal scale for (a,b) and (c,d). In the case with symmetry-breaking disorder, the multidomain protocol performs much better than the single-domain one, due to its shorter transfer time. Unlike the Creutz ladder version, it also always outperforms the trivial chain protocol, given that it has the same amount of degrees of freedom. Sigmoid functions fitted to the data are provided as a guide for the eye. Transfer times for  $L = 13, 12$  are  $t_{\text{tr}} = 332.3, 156.5, 55.9$  for the trivial chain and the single- and four-domain SSH chain, respectively. In the same order, the times for  $L = 21, 20$  are  $t_{\text{tr}} = 800.5, 2175.4, 55.9$ .

## V. CONCLUSIONS

In this work, we analyze the control possibilities that magnetic interference provides in the multidomain Creutz ladder, and propose a controlled particle transfer protocol between any two of the topological interphases in the model. Additionally, we also demonstrate that an exponential speed-up with respect to single-domain protocols can be achieved by employing the protected states in domain walls as signal amplifiers, both in the SSH chain and in the Creutz ladder. Future prospects for our work include the implementation of more complex protocols acting on the boundary states, and the study of the different quantum information applications that such our protocols have, such as braiding, entanglement generation or remote quantum gates.

## ACKNOWLEDGMENTS

J.Z. would like to thank Álvaro Gómez León, David Fernández and Jordi Picó Cortés for fruitful discussions. C.E.C. was supported by the Universidad Complutense de Madrid through Grant No. FEI-EU-19-12. G.P. and J.Z. were supported by Spain's MINECO through Grant No. PID2020-117787GB-I00 and by CSIC Research Platform PTI-001. J.Z. recognizes the FPU program FPU19/03575.

### Appendix A: Topological state preparation

The left, right and  $\mathcal{S}$ -type topological states of the rungless Creutz ladder, which are localized in two sites, can be prepared starting from a particle confined to a single site, while retaining topological protection. To do this, the hopping amplitudes of the given site with its neighbours must start off at zero, and have to be turned on adiabatically until they reach the value of the rest of the hopping amplitudes, with the appropriate complex phases. The symmetry protection is retained during this process, because the state corresponds to a topological state of a rhomboid CSSH ladder of varying  $J/J'$  [64]. Although the full system is not equivalent to the CSSH ladder during the preparation, it is locally equivalent to it around the computational states. Given the localized nature of all eigenstates during the protocol due to AB caging, this local equivalence is enough to make the computational state completely analogous to its CSSH ladder counterpart, including the topological protection, so the preparation protocol will be symmetry-protected against off-diagonal disorder.

### Appendix B: Transfer protocols inside the protected manifold

As explained above, the protected boundary states at the ends and walls of the models form an effective 1D chain. The left-to-right transfer is reduced to the problem of how to transfer a particle from the first to the last site in this effective 1D chain. Multiple avenues could be explored here, like for example imposing an additional dimerization between the domain walls, in the spirit of [42] to try and obtain an additional degree of protection, or considering the –also especially resilient– adiabatic passage protocol recently proposed in a two-domain SSH chain [43]. However, in this work we constrain our study to the simplest version of these protocols, given that it provides an exponential speed-up over the single-domain case: the modulation of the effective hopping amplitudes over time.

Among all possible ways to modulate them, we have chosen to follow the pulse form detailed in Eq. (16) for the control parameter  $c$  (which can be  $c = \epsilon, m$  or  $v$ , depending on the model) simultaneously in all domains,

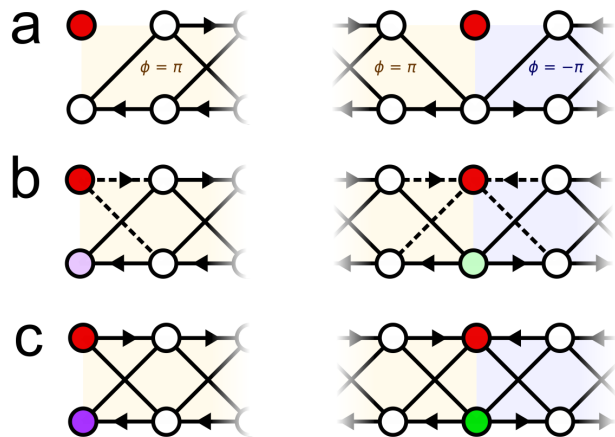


Figure 10. Preparation of the computational states  $|\mathcal{L}\rangle$  (left of the figure) and  $|\mathcal{S}_1\rangle$  (right) in the Creutz ladder. (a) The initial state has a particle localized in a single site in leg A. (b) The hopping amplitudes connected to that site (dashed lines) must start at a value of zero, and then be adiabatically switched on, with the proper complex phases. This protocol is topologically protected by chiral symmetry, given that each intermediate state corresponds to a topological state in a CSSH ladder [64], to which the system is locally equivalent. (c) The final state is the corresponding computational state in the Creutz ladder. Magnetic interference will cause the site in leg B to acquire the necessary phase, represented by color. Red is used for phase 0, green for phase  $\pi/2$  and purple for phase  $-\pi/2$ .

but allowing for a different value of  $c_{\text{tr}}$  for each domain. A straightforward numerical simulation can easily provide the appropriate values of these control parameters in order to obtain a fidelity of  $f > 0.995$  in the shortest time possible, that is, in the first maximum of the last site occupation. We have considered a value of  $c_{\text{tr}}^{(1)}$  in the first and last domain, and then a different value  $c_{\text{tr}}^{(2)}$  for the second and penultimate, and so on.

This, in turn, creates different effective hopping amplitudes in the effective Hamiltonian. We label here their values in the middle of the protocol as  $v_1$  for the first and last domains,  $v_2$  for the second and penultimate, and so forth.

We include a detailed list of all protocols with  $N > 2$  that were used in this work, together with all their parameters, in Table I.

### Appendix C: Runged vs. imbalanced Creutz ladder: symmetries and states

In this Appendix, we discuss the differences and similarities between the imbalanced ( $\epsilon \neq 0, m = 0$ ) and the rungless ( $m \neq 0, \epsilon = 0$ ) Creutz ladders.

The rungless, balanced regime ( $m = \epsilon = 0$ ) of the CL belongs to the BDI class as long as  $\phi \neq 0 \pmod{2\pi}$ , with a hidden chiral symmetry that can be expressed as

Model	Ref.	$N$	$\ell$	$L$	$c_{\text{tr}}^{(1)}$	$c_{\text{tr}}^{(2)}$	$c_{\text{tr}}^{(3)}$	$t_{\text{tr}}$	$t'_{\text{tr}}$
ICL	Fig. 5	3	4	16	1	0.952	–	123.4	30
ICL	Fig. 5	4	4	21	1	0.969	–	135.7	30
ICL	Fig. 5	5	4	26	1	0.973	–	148.9	30
ICL	Fig. 5	6	4	31	1	0.975	0.979	162.2	30
ICL	Fig. 6	4	2	13	1	0.906	–	63.1	30
SSH	Fig. 7	3	4	16	0.5	0.543	–	50.6	15
SSH	Fig. 7	4	4	21	0.5	0.560	–	55.9	15
SSH	Fig. 7	5	4	26	0.5	0.561	0.566	62.2	15
SSH	Fig. 7	6	4	31	0.5	0.563	0.576	67.5	15
SSH	Fig. 9	4	2	13	0.5	0.560	–	35.0	15

Table I. Multidomain transfer protocol parameters. We indicate the model in which they are implemented (ICL = imbalanced Creutz ladder, SSH = SSH chain), one of the Figs. which reference them, and the values of all parameters. The control parameter ( $v$  in SSH,  $\epsilon$  in ICL) is represented by  $c$ .

$\mathcal{X}_S^{(4)} = \text{diag}(\mathbb{1}_2, -\mathbb{1}_2)$  if we choose a four-site unit cell [64]. The rungless case also belongs to the BDI class if  $\phi = \pi \pmod{2\pi}$ , with different symmetries than in the previous case. The chiral symmetry is then  $\mathcal{X}_C = i\sigma_y$ . The imbalanced CL belongs to the AIII class if  $\phi = \pi$

mod  $2\pi$ , with the same chiral symmetry  $\mathcal{X}_C$ . When either of the control parameters ( $m$  or  $\epsilon$ ) is nonzero and  $\phi \neq 0, \pi \pmod{2\pi}$ , the system belongs to one of the nontopological symmetry classes in 1D. Topological edge states are still present in the model, but they are related only to crystalline symmetries instead [39].

Topological states are protected by these chiral symmetries, but not for all types of disorder. Diagonal (on-site) disorder always breaks the symmetries of the models, while each of the symmetries protects against different kinds of off-diagonal disorder, as shown in Table II. The system is only topologically protected if the off-diagonal disorder does not depend on the internal coordinate  $\sigma$ . For this reason, implementations that use a synthetic dimension for the two legs will most likely be advantageous over those using two real dimensions, given that the inter-cell parameters will be more correlated in the former case.

Crucially, fluctuations in any of the control parameters ( $m$  or  $\epsilon$ ) preserve the chiral symmetry  $\mathcal{X}_C$ , and thus the topological protection.

The rungless multidomain CL with rungless domain walls has the following topological states:

$$|\mathcal{L}\rangle = -\mathcal{N}_{\mathcal{L}} \sum_{j=1}^{\ell+1} \left(-\frac{2J}{m}\right)^{-j} |j\rangle \otimes \begin{pmatrix} 1 \\ -i \end{pmatrix} \quad (\text{C1})$$

$$|\mathcal{R}\rangle = -\mathcal{N}_{\mathcal{R}} \sum_{j=L-\ell}^L \left(-\frac{2J}{m}\right)^{j-L-1} |j\rangle \otimes \begin{pmatrix} 1 \\ (-1)^{N+1}i \end{pmatrix} \quad (\text{C2})$$

$$\begin{aligned} |\mathcal{P}_k\rangle &= -\mathcal{N}_{\mathcal{P}_k} \sum_{j=(k-1)(\ell+1)+2}^{k(\ell+1)} \left(-\frac{2J}{m}\right)^{j-k(\ell+1)-1} |j\rangle \otimes \begin{pmatrix} 1 \\ (-1)^{k+1}i \end{pmatrix} \\ &+ \mathcal{N}_{\mathcal{P}_k} \sum_{j=k(\ell+1)+2}^{(k+1)(\ell+1)} \left(-\frac{2J}{m}\right) |j\rangle \otimes \begin{pmatrix} 1 \\ (-1)^{k+1}i \end{pmatrix}, \end{aligned} \quad (\text{C3})$$

and its effective Hamiltonian has the same form as the imbalanced case, with the following hopping amplitudes:

$$v_k = 2(-1)^{k+p_{k-1}} im \mathcal{N}_k \mathcal{N}_{k-1} \left(-\frac{2J}{m}\right)^{-d-2}, \quad (\text{C4})$$

where  $d$  is the distance between the maxima of the involved states, and  $p_{k-1} = 0$  if the  $(k-1)$ -th state is a  $\mathcal{P}$  state, and  $p_{k-1} = 1$  otherwise.

In a transfer involving an  $\mathcal{S}$  state that extends to the left or right, this state will take the form:

$$|\mathcal{S}_k\rangle_{\text{left}} = -\mathcal{N}_{\mathcal{S}_k} \sum_{j=(k-1)(\ell+1)+2}^{k(\ell+1)} \left(-\frac{2J}{m}\right)^{j-k(\ell+1)-1} |j\rangle \otimes \begin{pmatrix} 1 \\ (-1)^{k+1}i \end{pmatrix} \quad (\text{C5})$$

$$|\mathcal{S}_k\rangle_{\text{right}} = -\mathcal{N}_{\mathcal{S}_k} \sum_{j=k(\ell+1)+2}^{(k+1)(\ell+1)} \left(-\frac{2J}{m}\right)^{k(\ell+1)-j+1} |j\rangle \otimes \begin{pmatrix} 1 \\ (-1)^{k+1}i \end{pmatrix}. \quad (\text{C6})$$

The acquired phases in a transfer jumping over  $n_w$  walls with a domain length of  $\ell$  are different from the

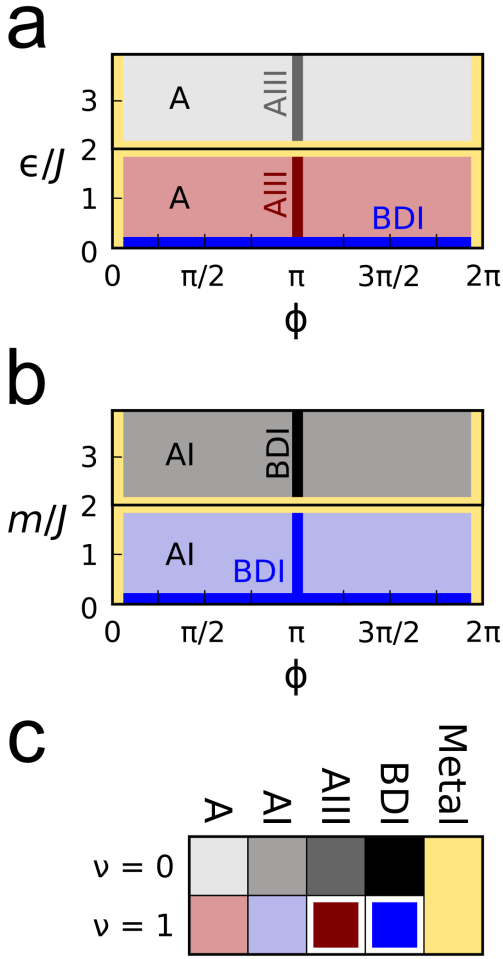


Figure 11. Phase diagrams showing the symmetry classes and winding numbers of the two Creutz ladder variants. (a) Imbalanced Creutz ladder phase diagram, with  $m = 0$ . (b) Runged Creutz ladder phase diagram, with  $\epsilon = 0$ . (c) Color code for the symmetry classes and winding number values ( $\nu$ ). Topological phases explained by the Altland-Zirnbauer classification [45] are indicated by a white outline.

imbalanced case, and can only be 0 or  $\pi$ , making it easier to compensate if needed for quantum information applications:

$$\zeta(\ell, n_w, x, \varsigma) = \begin{cases} (-1)^{\ell+n_w/2+\delta-x, \varsigma} & \text{for even } n_w \\ (-1)^{(n_w-1)/2} & \text{for odd } n_w, \end{cases} \quad (\text{C7})$$

where  $x = \pm 1$  is the chirality of the leftmost transferred state,  $\varsigma$  is the direction of transfer ( $\pm 1$  for left-to-right/right-to-left).

Apart from the phases, the rest of the dynamics of the model are identical to those in the imbalanced CL. In particular, all transfer times are the same, described by Eqs. (20,21), with  $m$  playing the part of  $\epsilon$ . This was confirmed both analytically and numerically.

	$\delta J_{h/d}(j, \sigma)$	$\delta J(j)$	$\delta \phi(j, \sigma)$	$\delta c(j)$	$\delta \mu^*$
$\mathcal{X}_C = \sigma_y$ [ $\phi = \pm \pi$ ]		✓		✓	
$\mathcal{X}_S^{(4)} = \text{diag}(\mathbb{1}_2, -\mathbb{1}_2)$ [ $m = \epsilon = 0$ ]	✓	✓	✓		

Table II. Types of disorder and the chiral symmetries in the Creutz ladder that are preserved (✓) or broken by them. The regime in which the symmetry is present is shown in square brackets. The dependence of the disorder terms is indicated in parentheses.  $\delta J_{h/d}(j, \sigma)$  allows for fluctuations of different value in each of the four inter-cell links, while  $\delta J(j)$  means that we apply the same fluctuation to all four inter-cell hopping terms.  $\delta c(j)$  represents a rung-dependent disorder in one of the control parameters: the vertical links ( $c = m$ ) or the energy imbalance ( $c = \epsilon$ ),  $\delta \phi(j, \sigma)$  indicates a bond-dependent fluctuation of the Peierls phases, and  $\delta \mu^*$  stands for a general non-homogeneous fluctuation in the chemical potentials. For a detailed description of all symmetries, see [64].

#### Appendix D: Robustness against disorder: factors and phases

In this Appendix, we elaborate on the results obtained for the disordered protocols. We discuss the factors that can affect the performance of the protocol, the highly robust behaviour of the acquired phase, and its effect on the transfer of a superposition of states.

There are three main factors which determine the robustness against disorder of a given protocol:

- The **topology** of the system. When at least one protecting symmetry is preserved, the fidelity of the protocol is better in the topological case, all else being equal. Additionally, the phase of the wavefunction components is preserved especially well, even if the protecting symmetries are broken. This is relevant in the CL, due to the chiralities being defined by the relative phase between the two legs, and also for more complex protocols, where relative phases between different computational states carry information.
- The number of **degrees of freedom**. More complicated models like the CL, with a larger amount of moving parts, can induce more errors in the protocol for the same level of disorder. However, the relative increase in errors will be platform-dependent, given that some parameters of the Hamiltonian (and their errors) can be correlated in some experimental realizations but not in others.
- The **speed of the protocol**. Due to the accumulation of errors, protocols that take more time usually have a lower fidelity than their faster counterparts, all else being equal.

As mentioned in the main text, the value of the acquired phase in the transfer,  $\zeta$ , is exceptionally robust in the presence of disorder. This is because it is a geometric

phase, not a dynamical phase, and so small changes in the transfer time do not affect its value. We investigate this by representing the circular standard deviation [65] of the acquired phase values over 1000 realizations.

In the case of symmetry-preserving disorder, the acquired phases are almost completely unperturbed for disorder strengths of more than 20% of the energy scale of the model in both the SSH chain and CL protocols, with only the single-domain CL protocol showing the effects of disorder near  $\delta J \simeq 0.15$ . This protection does not seem to carry over to the general disorder case, but we see a better performance in the faster, four-domain SSH and Creutz models than in a single-domain or trivial protocol, even in the case where the fidelity in the CL did not outperform the trivial chain, compare Fig. 12 (d) with Fig. 6 (d). In general, the stability of the acquired phase seems to outlast the fidelity plateau as disorder increases.

This behaviour is useful in situations where the predictability of the phase is desired, like quantum information implementations in which the topological model is coupled to external qubits (e.g., if used as a photonic communication line to implement remote quantum gates, like in [7]), or more complex transfer protocols where relative phases between boundary states also have to be preserved.

To show a simple example of the latter, we consider the transfer of a superposition of states from the two leftmost to the two rightmost computational states in a six-domain Creutz ladder with  $L = 31$ :

$$|+\text{left}^{\text{CL}}\rangle = (|\mathcal{L}\rangle + |\mathcal{S}_1\rangle)/\sqrt{2} \rightarrow \quad (\text{D1})$$

$$\rightarrow |\psi_f^{\text{CL}}\rangle = |-\text{right}^{\text{CL}}\rangle = \zeta_1 |\mathcal{S}_5\rangle + \zeta_2 |\mathcal{R}\rangle. \quad (\text{D2})$$

This is achieved with two successive transfer protocols [see Fig. 13 (b)]. The acquired phase factors are  $\zeta_1 = -1, \zeta_2 = 1$ . We use  $t_{\text{prep}} = t'_{\text{prep}} = 30$ ,  $\epsilon_{\text{tr}}^{(1)} = J = 1$ ,  $\epsilon_{\text{tr}}^{(2)} = \epsilon_{\text{tr}}^{(3)} = 0.97$ , and a total transfer time of  $T_{\text{tr}} = 391.4$  for the whole protocol. The fidelity of the transferred state for each system at the final time  $t_f$ ,  $F = |\langle \psi_f^{(\text{ideal})} | \psi(t_f) \rangle|^2$ , is  $F = 0.996$  for the pristine system.

As a topologically trivial protocol to compare against, we use a transmission line consisting of a 1D chain of sites with a hopping amplitude of  $J = 1$ , of the same length as each of the transfers in the CL, and with two sites at the left ( $|1, a/b\rangle$ ) and right ( $|L, a/b\rangle$ ) ends [see Fig. 13 (a)]. The initial state is  $|+\text{left}^{\text{triv}}\rangle = (|1, a\rangle + |1, b\rangle)/\sqrt{2}$ , and two successive transfers are implemented using the same chain, until the final state,  $|\psi_f^{\text{triv}}\rangle = |+\text{right}^{\text{triv}}\rangle = (|L, a\rangle + |L, b\rangle)/\sqrt{2}$  (plus a certain global phase), is achieved. An initial chemical potential of  $-\mu_0 = -10J$  is set on the four end sites, and the optimal transfer time for the full protocol was found to be  $T_{\text{tr}} = 2405.6$  (with  $F = 0.986$ ).

We now obtain the fidelity average over 1000 realizations for both symmetry-preserving disorder, defined in Eq. (22), and general disorder, see Eqs. (23,24). The

results are shown in Fig. 14. The topological protocol shows a plateau up to disorders of  $0.15J$  in the former case, and still outperforms the trivial protocol in the latter case, for low levels of disorder. The trivial protocol falls quickly to  $F = 0.5$  in both cases as disorder is turned on, given that the relative phase of the final superposition is almost random even for small disorder values, while the phases in the topological protocol are more reliable. In the case of general disorder, this is mainly due to the much shorter times of the CL protocol.

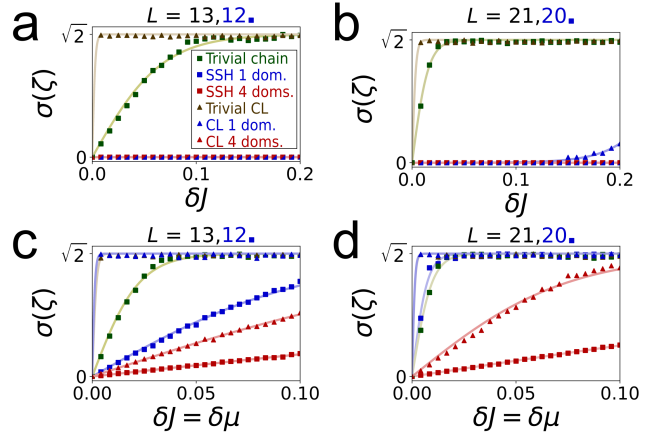


Figure 12. Standard deviation of the acquired phases over 1000 realizations of six different protocols, for symmetry-preserving (a,b) and general (c,d) disorder. The lengths of the models are  $L = 13$ (a,c) and  $21$  (b,d) ( $L = 12, 20$  for the single-domain SSH chain). The four topological protocols show almost perfect results for symmetry-preserving disorder up to  $0.2J$ . In the case of general disorder, the four-domain protocols show a clear advantage over the rest, especially for  $L = 21$ , due to their shorter transfer times. Continuous lines fitted to the points are added as a guide for the eye.

### Appendix E: The multidomain SSH chain effective Hamiltonian

The boundary states in the multidomain SSH chain have the form:

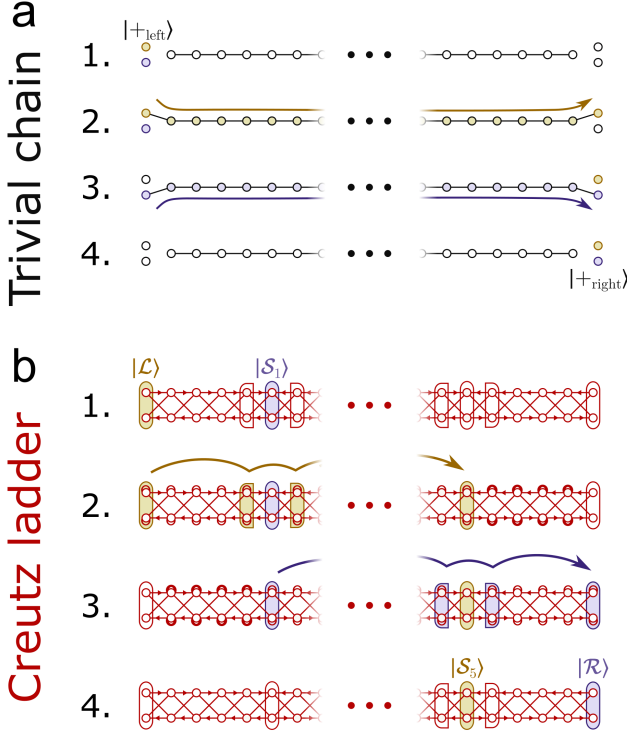


Figure 13. Transfer of a particle in a superposition of two states. The amplitude in each of the two states is transferred separately. (a) Transfer protocol in a trivial chain with  $L = 26$  for a particle superposed between two sites. The transfer is induced by using wells of chemical potential at both edges. (b) Transfer protocol in a six-domain,  $L = 31$  Creutz ladder for the superposition of two computational states. Each of the computational states is translated 26 rungs to the right. The first transferred state acquires an additional  $\pi$  phase in the CL protocol.

$$|\mathcal{L}\rangle = -\mathcal{N}'_{\mathcal{L}} \sum_{x=1}^{\ell+1} \left(-\frac{w}{v}\right)^{-x} |x, a\rangle \quad (\text{E1})$$

$$|\mathcal{R}\rangle = -\mathcal{N}'_{\mathcal{R}} \sum_{x=L-\ell}^L \left(-\frac{w}{v}\right)^{x-[L/2]-1} |x, \Delta_N\rangle \quad (\text{E2})$$

$$|\mathcal{S}_k\rangle = \mathcal{N}'_{\mathcal{S}_k} \left[ |x_0^{(k)}, \Delta_k\rangle + \sum_{x=x_0^{(k)}-\ell/2}^{x_0^{(k)}-1} \left(-\frac{w}{v}\right)^{x-x_0^{(k)}} |x, \Delta_k\rangle + \sum_{x=x_0^{(k)}+1}^{x_0^{(k)}+\ell/2} \left(-\frac{w}{v}\right)^{x_0^{(k)}-x} |x, \Delta_k\rangle \right], \quad (\text{E3})$$

where  $x_0^{(k)} = \lceil [k(\ell+1)+1]/2 \rceil$  is the unit cell where the  $k$ -th domain wall is, and  $\Delta_k = a$  (b) if  $k$  is even (odd). The effective Hamiltonian for the boundary states in the SSH chain has the same form as Eq. (14), but substituting all  $\mathcal{P}$  states –which do not exist here– by  $\mathcal{S}$  states.

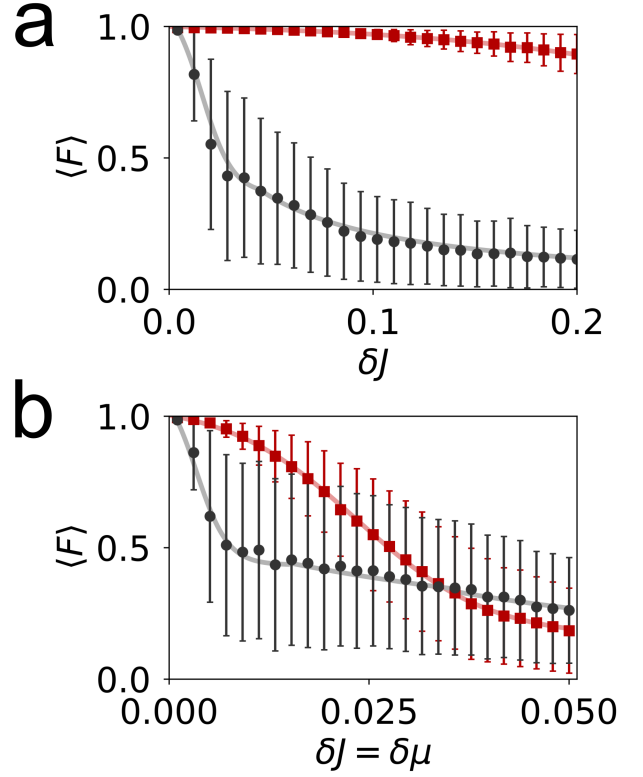


Figure 14. Average value of the fidelity of the transferred superposed state over 1000 realizations in the presence of (a) symmetry-preserving [see Eq. (22)] and (b) general disorder [Eqs. (23,24)], using a trivial chain (black) and a six-domain topological CL (red). Note the different horizontal scale between the figures. We include its standard deviation as error bars. The CL protocol outperforms the trivial one by a wide margin in case (a), but it is also better at low levels of disorder in case (b). This is due to the robustness of the relative phase in the topological protocol, thanks to its shorter transfer time. In the trivial case, the relative phase is soon lost, making the fidelity quickly fall to  $\sim 0.5$ .

The effective hopping amplitudes now have the form:

$$t_1 = v\mathcal{N}'_{\mathcal{L}}\mathcal{N}'_{\mathcal{S}_1} \left(-\frac{w}{v}\right)^{-\ell/2-1} \quad (\text{E4})$$

$$t_k = -v\mathcal{N}'_{\mathcal{S}_k}\mathcal{N}'_{\mathcal{S}_{k-1}} \left(-\frac{w}{v}\right)^{-\ell/2}, \quad k = 2, \dots, N-1 \quad (\text{E5})$$

$$t_N = v\mathcal{N}'_{\mathcal{R}}\mathcal{N}'_{\mathcal{S}_{N-1}} \left(-\frac{w}{v}\right)^{-\ell/2-1}, \quad (\text{E6})$$

where the normalization constants can be approximated as:

$$\mathcal{N}'_{\mathcal{L}} = \mathcal{N}'_{\mathcal{R}} = \sqrt{w^2/v^2 - 1} \quad (\text{E7})$$

$$\mathcal{N}'_{\mathcal{S}_k} = \sqrt{\frac{w^2 - v^2}{w^2 + v^2}} \quad \forall k. \quad (\text{E8})$$



- 
- [1] J. Preskill, *Quantum* **2**, 79 (2018).
- [2] N. Y. Yao, C. R. Laumann, A. V. Gorshkov, H. Weimer, L. Jiang, J. I. Cirac, P. Zoller, and M. D. Lukin, *Nature Communications* **4**, 1585 (2013).
- [3] C. Dlaska, B. Vermersch, and P. Zoller, *Quantum Science and Technology* **2**, 015001 (2017).
- [4] M. A. Lemonde, V. Peano, P. Rabl, and D. G. Angelakis, *New Journal of Physics* **21**, 113030 (2019).
- [5] M. Bello, C. E. Creffield, and G. Platero, *Physical Review B* **95**, 094303 (2017).
- [6] M. Leijnse and K. Flensberg, *Physical Review Letters* **107**, 210502 (2011).
- [7] N. Lang and H. P. Büchler, *npj Quantum Information* **3**, 47 (2017).
- [8] L. Jin, P. Wang, and Z. Song, *Scientific Reports* **7**, 5903 (2017).
- [9] M. P. Estarellas, I. D’Amico, and T. P. Spiller, *Scientific Reports* **7**, 42904 (2017).
- [10] F. Mei, G. Chen, L. Tian, S. L. Zhu, and S. Jia, *Physical Review A* **98**, 012331 (2018).
- [11] P. Boross, J. K. Asbóth, G. Széchenyi, L. Oroszlány, and A. Pályi, *Physical Review B* **100**, 045414 (2019).
- [12] C. Yuce, *Physical Review A* **99**, 032109 (2019).
- [13] F. M. D’Angelis, F. A. Pinheiro, D. Guéry-Odelin, S. Longhi, and F. Impens, *Physical Review Research* **2**, 033475 (2020).
- [14] S. Tan, R. W. Bomantara, and J. Gong, *Physical Review A* **102**, 022608 (2020).
- [15] P. Comaron, V. Shahnazaryan, and M. Matuszewski, *Optics Express* **28**, 38698 (2020).
- [16] J. Cao, W. X. Cui, X. Yi, and H. F. Wang, *Annalen der Physik* **533**, 2100120 (2021).
- [17] Z. G. Chen, W. Tang, R. Y. Zhang, Z. Chen, and G. Ma, *Physical Review Letters* **126**, 054301 (2021).
- [18] N. E. Palaiodimopoulos, I. Brouzos, F. K. Diakonou, and G. Theocharis, *Physical Review A* **103**, 052409 (2021).
- [19] J. X. Han, J. L. Wu, Y. Wang, Y. Xia, Y. Y. Jiang, and J. Song, *Physical Review A* **103**, 032402 (2021).
- [20] J. Yuan, C. Xu, H. Cai, and D. W. Wang, *APL Photonics* **6**, 030803 (2021).
- [21] M. Creutz, *Physical Review Letters* **83**, 2636 (1999).
- [22] B. Song, L. Zhang, C. He, T. F. J. Poon, E. Hajiyev, S. Zhang, X. J. Liu, and G. B. Jo, *Science Advances* **4** (2018).
- [23] J. Hyoun Kang, J. Ho Han, and Y. Shin, *New Journal of Physics* **22**, 013023 (2020).
- [24] Y. He, R. Mao, H. Cai, J. X. Zhang, Y. Li, L. Yuan, S. Y. Zhu, and D. W. Wang, *Physical Review Letters* **126**, 103601 (2021), arXiv:2010.06782.
- [25] H. Alaeian, C. W. S. Chang, M. V. Moggaddam, C. M. Wilson, E. Solano, and E. Rico, *Physical Review A* **99**, 053834 (2019).
- [26] J. S. C. Hung, J. H. Busnaina, C. W. S. Chang, A. M. Vadiraj, I. Nsanzineza, E. Solano, H. Alaeian, E. Rico, and C. M. Wilson, *Physical Review Letters* **127**, 100503 (2021).
- [27] S. Mukherjee, M. Di Liberto, P. Öhberg, R. R. Thomson, and N. Goldman, *Physical Review Letters* **121**, 075502 (2018), arXiv:1805.03564.
- [28] J. Vidal, R. Mosseri, and B. Douçot, *Physical Review Letters* **81**, 5888 (1998).
- [29] C. E. Creffield and G. Platero, *Physical Review Letters* **105**, 086804 (2010).
- [30] M. Bello, C. E. Creffield, and G. Platero, *Scientific Reports* **6**, 22562 (2016).
- [31] J. Jünemann, A. Piga, S. J. Ran, M. Lewenstein, M. Rizzi, and A. Bermudez, *Physical Review X* **7**, 031057 (2017).
- [32] M. Tovmasyan, E. P. Van Nieuwenburg, and S. D. Huber, *Physical Review B* **88**, 220510 (2013).
- [33] S. Takayoshi, H. Katsura, N. Watanabe, and H. Aoki, *Physical Review A* **88**, 063613 (2013).
- [34] O. Derzhko, J. Richter, and M. Maksymenko, *International Journal of Modern Physics B* **29**, 1530007 (2015).
- [35] N. Roy, A. Ramachandran, and A. Sharma, *Physical Review Research* **2**, 043395 (2020).
- [36] H. Nakai and C. Hotta, *Nature Communications* **13**, 579 (2022).
- [37] M. Röntgen, C. V. Morfonios, I. Brouzos, F. K. Diakonou, and P. Schmelcher, *Physical Review Letters* **123**, 080504 (2019).
- [38] Y. Kuno, T. Orito, and I. Ichinose, *New Journal of Physics* **22**, 013032 (2020).
- [39] L. Li and S. Chen, *Physical Review B* **92**, 085118 (2015).
- [40] J. Zurita, C. E. Creffield, and G. Platero, *Advanced Quantum Technologies* **3**, 1900105 (2019).
- [41] W. P. Su, J. R. Schrieffer, and A. J. Heeger, *Physical Review B* **22**, 2099 (1980).
- [42] F. Munoz, F. Pinilla, J. Mella, and M. I. Molina, *Scientific Reports* **8**, 1 (2018).
- [43] S. Longhi, *Physical Review B* **99**, 155150 (2019), arXiv:1904.08087.
- [44] L. Qi, Y. Yan, Y. Xing, X. D. Zhao, S. Liu, W. X. Cui, X. Han, S. Zhang, and H. F. Wang, *Physical Review Research* **3**, 023037 (2021).
- [45] A. Altland and M. R. Zirnbauer, *Physical Review B* **55**, 1142 (1997).
- [46] N. Sun and L.-K. K. Lim, *Physical Review B* **96**, 035139 (2017).
- [47] Actually, their overlap (e.g.  $\langle \mathcal{L} | \mathcal{P} \rangle$ ) is always zero due to their different chiralities, but the effective hopping amplitude between them ( $\langle \mathcal{L} | \mathcal{H} | \mathcal{P} \rangle$ ) is not. We employ this slight abuse of language throughout the paper for convenience.
- [48] A. Alase, E. Cobanera, G. Ortiz, and L. Viola, *Physical Review B* **96**, 195133 (2017).
- [49] E. Cobanera, A. Alase, G. Ortiz, and L. Viola, *Physical Review B* **98**, 245423 (2018).
- [50] S. Longhi, G. L. Giorgi, and R. Zambrini, *Advanced Quantum Technologies* **2**, 1800090 (2019).
- [51] E. Knill, *Nature* **434**, 39 (2005).
- [52] D. S. Wang, A. G. Fowler, and L. C. Hollenberg, *Physical Review A* **83**, 020302(R) (2011).
- [53] A. G. Fowler, A. C. Whiteside, and L. C. Hollenberg, *Physical Review Letters* **108**, 180501 (2012).
- [54] L. Egan, D. M. Debroy, C. Noel, A. Risinger, D. Zhu, D. Biswas, M. Newman, M. Li, K. R. Brown, M. Cetina, and C. Monroe, (2020), arXiv:2009.11482.
- [55] All transfer protocols detailed in our work are actually bidirectional, that is, they can be used to swap the two components of the involved states. In a bidirectional transfer, the component travelling from left to right will

- acquire a phase of  $\zeta(\ell, n_w, x, 1)$ , while the component traveling from right to left will get  $\zeta(\ell, n_w, x, -1)$ .
- [56] This is reminiscent of the way topological domains are created in the SSH chain, see Section IV for more details.
- [57] As discussed in [7], a value of the control parameter closer to the topological phase transition can be used to speed up the protocol, but this also reduces the gap, making it more susceptible to noise, and requires a really precise control in order not to cross the phase transition point accidentally when speeding up the protocols to the point needed in large systems.
- [58] D. Porras and S. Fernández-Lorenzo, *Physical Review Letters* **122**, 143901 (2019).
- [59] C. C. Wanjura, M. Brunelli, and A. Nunnenkamp, *Nature Communications* **11**, 3149 (2020).
- [60] T. Ramos, J. J. García-Ripoll, and D. Porras, *Physical Review A* **103**, 033513 (2021).
- [61] C. C. Wanjura, M. Brunelli, and A. Nunnenkamp, *Physical Review Letters* **127**, 213601 (2021).
- [62] T. Ramos, Á. Gómez-León, J. J. García-Ripoll, A. González-Tudela, and D. Porras, (2022), arXiv:2207.13728.
- [63] Á. Gómez-León, T. Ramos, A. González-Tudela, and D. Porras, (2022), arXiv:2207.13715.
- [64] J. Zurita, C. Creffield, and G. Platero, *Quantum* **5**, 591 (2021).
- [65] The circular standard deviation of a set of data  $\{\zeta_j\}_{j=1}^M$  can be found as  $\sigma(\zeta) = \sqrt{2 \left(1 - \left| \sum_{j=1}^M e^{i\zeta_j} \right| \right)}$ . It is needed to take into account the periodicity of the phases, and it ranges between 0 and  $\sqrt{2}$ .